

RESEARCH ARTICLE

MSLAU-Net: A Hybrid CNN-Transformer Network for Medical Image Segmentation

Libin Lan¹ | Yanxin Li¹ | Xiaojuan Liu² | Juan Zhou³ | Jianxun Zhang² | Nannan Huang^{4,5,6} | Yudong Zhang⁷¹College of Computer Science and Engineering, Chongqing University of Technology, Chongqing, China²College of Artificial Intelligence, Chongqing University of Technology, Chongqing, China³Department of Pharmacy, the Second Affiliated Hospital of Army Military Medical University, Chongqing, China⁴Department of Prosthodontics, the Affiliated Stomatological Hospital of Chongqing Medical University, Chongqing, China⁵Chongqing Key Laboratory of Oral Diseases, Chongqing, China⁶Chongqing Municipal Key Laboratory of Oral Biomedical Engineering of Higher Education, Chongqing, China⁷School of Computer Science and Engineering, Southeast University, Nanjing, China

Correspondence

Libin Lan, College of Computer Science and Engineering, Chongqing University of Technology, Chongqing 400054, China.

Email: lanlbn@cqut.edu.cn

Abstract

Accurate medical image segmentation allows for the precise delineation of anatomical structures and pathological regions, which is essential for treatment planning, surgical navigation, and disease monitoring. Both CNN-based and Transformer-based methods have achieved remarkable success in medical image segmentation tasks. However, CNN-based methods struggle to effectively capture global contextual information due to the inherent limitations of convolution operations. Meanwhile, Transformer-based methods suffer from insufficient local feature modeling and face challenges related to the high computational complexity caused by the self-attention mechanism. To address these limitations, we propose a novel hybrid CNN-Transformer architecture, named MSLAU-Net, which integrates the strengths of both paradigms. The proposed MSLAU-Net incorporates two key ideas. First, it introduces Multi-Scale Linear Attention, designed to efficiently extract multi-scale features from medical images while modeling long-range dependencies with low computational complexity. Second, it adopts a top-down feature aggregation mechanism, which performs multi-level feature aggregation and restores spatial resolution using a lightweight structure. Extensive experiments conducted on benchmark datasets covering three imaging modalities demonstrate that the proposed MSLAU-Net outperforms other state-of-the-art methods on nearly all evaluation metrics, validating the superiority, effectiveness, and robustness of our approach. Our code is available at <https://github.com/Monsoon49/MSLAU-Net>.

KEYWORDS

convolutional neural network, linear attention, medical image segmentation, MSLAU-Net, transformer

1 | INTRODUCTION

Medical image analysis plays a pivotal role in computer-aided diagnosis and modern medical practice [7, 6]. Central to this process is robust and efficient medical image segmentation, which provides a foundation for accurate diagnosis, treatment planning, and disease monitoring [13, 39]. Advanced computational methods, such as convolutional neural networks (CNNs) and transformers, enhance segmentation reliability by ensuring consistent extraction of clinically relevant insights from complex data. These techniques not only improve diagnostic accuracy but also offer critical applications in tracking disease progression and guiding preventive care strategies.

In recent years, CNNs have achieved significant success in medical image segmentation. The fully convolutional network (FCN) [29] pioneers this advancement, but limitations in detail preservation and contextual understanding restrict its broader applicability. To address these challenges, U-Net [36] introduces an encoder-decoder architecture with skip connections, thereby effectively retaining finer details and improving accuracy. This design is particularly well-suited for medical image segmentation tasks, enabling the precise identification and localization of fine structures within target regions. Building on the achievements of U-Net, numerous U-shaped architectures have been developed, such as 3D U-Net [10], V-Net [31], U-Net++ [46], and DenseUNet [27]. Despite their proven success in medical image segmentation, CNN-based methods are inherently constrained by the fixed receptive fields of convolutional

kernels, hindering their capacity to capture spatial long-range dependencies and global semantic information. To address this limitation, several studies have proposed employing dilated convolutions [9, 22, 8, 15], self-attention mechanisms [37, 42], and image pyramid frameworks [44, 33]. Despite these efforts, effectively capturing long-range spatial dependencies remains a persistent challenge for such methods.

Inspired by the success of transformers in natural language processing (NLP) [41] and computer vision [12], the self-attention mechanism has garnered significant attention for its ability to capture global dependencies and emphasize critical features in medical imaging. Several representative studies, such as nnFormer [45], UTNet [14], TransUNet [7], HiFormer [19] and MISSFormer [21], have focused on integrating transformers into medical image segmentation tasks. However, vanilla self-attention mechanisms suffer from high computational complexity and memory demands, limiting their broad applicability and efficiency in medical image segmentation tasks.

To address these challenges, various modifications have been proposed. Among them, sparse attention mechanisms are frequently proposed as an effective solution to mitigate these constraints, with notable methods including Swin-Unet [6], Gated Axial UNet (MedT) [40], BRAU-Net [5], and BRAU-Net++ [24]. Despite their effectiveness, sparse attention typically restricts the receptive field by focusing only on a small portion of the input sequence or elements within a predefined window. This limitation risks neglecting critical long-range positions, resulting in an incomplete representation of the overall context. In contrast, linear attention offers greater flexibility and enables the capture of broader global dependencies. Specifically, linear attention approximates the original Softmax function using feature mapping or mathematical transformations and exploits the associativity of matrix multiplication to reorder computations from $(QK)V$ to $Q(KV)$ [3, 16, 17]. By doing so, the computational complexity is effectively reduced to $\mathcal{O}(N)$. However, to the best of our knowledge, the application of linear attention to medical image segmentation remains underexplored, motivating us to investigate its potential in this domain.

Multi-scale learning [8, 44, 35] and global receptive fields [43] are widely recognized as critical factors for enhancing model segmentation performance [4]. While linear attention inherently satisfies the need for global contextual understanding, most existing linear attention approaches operate at a single scale, failing to fully exploit multi-scale information. However, it is well-known that multi-scale information is particularly important for medical image segmentation tasks, as it encapsulates both fine-grained details and high-level semantic patterns. This capability is essential for handling significant variations

between different tissues and lesion areas, ranging from microscopic cellular structures to macroscopic organ levels. To this end, we propose a novel **Multi-Scale Linear Attention (MSLA)** module, which integrates depth-wise convolutions at multiple scales to extract hierarchical features from input data and employs linear attention to aggregate cross-scale global context. This design simultaneously achieves scale-specific feature refinement and efficient global contextual modeling, ensuring comprehensive representation learning.

Using MSLA as a foundational building module, we design transformer-based Global Feature Extraction (GFE) blocks. Combining these GFE blocks with CNN-based Local Feature Extraction (LFE) blocks, adapted from the Local UniFormer block [26], we construct a four-stage encoder. In the first two stages, we utilize LFE blocks for local feature modeling, while in the last two stages, we employ GFE blocks (see Fig. 3) to capture global features. At its core, the GFE block integrates the MSLA module to enable multi-scale feature extraction and computationally efficient linear attention, ensuring robust hierarchical representation learning. For the decoder, instead of adopting conventional symmetric U-shaped architectures, we incorporate a top-down multi-level feature aggregation mechanism. This mechanism fuses features from the encoder stages using lightweight convolutional layers and bilinear upsampling operations, progressively enriching spatial details and semantic coherence during decoding. Built upon this encoder-decoder design, we propose **MSLAU-Net**, a hybrid architecture that synergizes the strengths of CNNs and transformers for efficient medical image segmentation.

Our main contributions are three-fold:

- We propose a novel MSLA module designed in a parallel architecture to fully leverage the strengths of CNNs for capturing multi-scale low-level fine-grained details and linear attention for modeling long-range dependencies. This design enables the model to simultaneously benefit from the local feature extraction and the global context understanding while maintaining low computational complexity, which is essential for improving both the computational efficiency and segmentation performance of the model.
- We design a top-down aggregation mechanism on the decoder side to aggregate multi-level features from the corresponding stages of the encoder. All aggregated features are then upsampled to recover the original spatial resolution. Building upon this aggregation mechanism and the proposed MSLA module, we introduce MSLAU-Net, a hybrid CNN-Transformer encoder-decoder architecture that adopts an asymmetric design instead of the conventional symmetric U-shaped networks, enabling the model to efficiently segment target regions.

- We extensively evaluate MSLAU-Net on three benchmark medical image datasets: Synapse Multi-Organ Segmentation [25], Automated Cardiac Diagnosis Challenge [2], and CVC-ClinicDB [1]. Experimental results demonstrate that MSLAU-Net achieves state-of-the-art performance with excellent generalization and robustness across diverse medical imaging tasks.

The remainder of this paper is organized as follows. Section 2 delves into the findings and limitations derived from previous relevant work. Section 3 illuminates our model’s design and architecture. Section 4 presents experimental results, visualizes MSLA attention maps, and provides an in-depth analysis of performance. Section 5 summarizes our findings, points out the limitations of the work, and outlines directions for future research.

2 | RELATED WORK

Our work is related to both CNN-based and transformer-based methods for medical image segmentation. In addition, a key contribution of our work is the improvement of the transformer’s core building module, i.e., the attention mechanism by proposing a novel linear attention module aimed at enhancing computational efficiency. Therefore, in this section, we will review relevant literature focusing on methods that apply CNNs and transformers to medical image segmentation tasks, as well as advancements in linear attention.

2.1 | Medical Image Segmentation

CNN-Based Methods. Initially, U-shaped networks developed for medical image segmentation utilized CNN operations to achieve precise results. U-Net [36] was the first to introduce this distinctive U-shaped architecture, designed to effectively obtain multi-scale information and fuse features (via skip connections), which makes it particularly well-suited for preserving local fine-grained details and capturing global semantic information. Since then, several variants have been proposed to further improve performance [46, 20, 10]. For instance, U-Net++ [46] introduces nested and dense skip connections to reduce the semantic gap between the encoder and decoder. UNet 3+ [20] optimizes full-scale skip connections and incorporates deep supervision to boost segmentation accuracy. Additionally, 3D-Unet [10] extends the original U-Net design by incorporating 3D convolutions into its architecture, which can effectively process volumetric medical data, such as CT and MRI scans. Owing to the powerful local feature representation capabilities of CNNs, CNN-based U-shaped architectures have

demonstrated exceptional effectiveness in medical image segmentation. However, convolutional operations are inherently limited in their ability to capture long-range dependencies. To address this limitation, we propose incorporating transformers into our model architecture to compensate for the shortcomings of CNNs. Specifically, we replace CNNs with transformers in the deeper encoding stages of our model.

Transformer-Based Methods. Motivated by the success of transformers in NLP [41], there has recently been growing interest in applying transformers to computer vision tasks [12, 47, 26], which has proven effective due to its ability to model long-range dependencies. As a result, more approaches have emerged that aim to leverage transformers for medical image analysis, particularly for medical image segmentation, which requires a comprehensive understanding of both structural details and global context [45, 14, 19, 21, 5, 18]. Transformer-based representative works in medical image segmentation include TransUNet [7], which integrates the merits of CNNs and transformers for local feature extraction and global contextual modeling, respectively, within a U-shaped architecture; Swin-Unet [6], which adopts a pure transformer architecture based on Swin Transformer [28], enabling efficient computation; and BRAU-Net++ [24], which innovatively introduces dynamic sparse attention into a hybrid CNN-Transformer architecture and redesigns skip connection by using channel-spatial attention mechanism. Despite these advancements, existing transformer-based methods often rely on Softmax attention or sparse attention mechanisms, which still present challenges such as high computational costs and limited receptive field sizes. In contrast to these approaches, we propose using linear attention to achieve lower computational complexity and provide a global receptive field, so as to overcome some of the limitations associated with Softmax and sparse attention mechanisms.

2.2 | Linear Attention

Contrary to sparse attention mechanisms, which have a restricted receptive field, linear attention reformulates the self-attention mechanism by employing kernel functions instead of Softmax functions with two main advantages. First, it reduces computational complexity to $\mathcal{O}(N)$ by leveraging the associative property of matrix multiplication to change the computation order. Second, it provides a global receptive field, allowing models to capture dependencies across entire inputs. The pioneering work [23] replaces the Softmax function with a mapping function ϕ applied to Q and K . However, relying solely on simple feature mappings can lead to substantial performance degradation. Therefore, several methods are proposed to design effective approximation techniques to address this issue. Efficient Attention [38] applies the Softmax function to

both \mathbf{Q} and \mathbf{K} , respectively. Hydra Attention [3] introduces the hydra trick and uses cosine similarity instead of the Softmax function. FLatten Transformer [16] proposes a simple mapping function called focused function and adopts a rank restoration module to preserve feature diversity. Agent Attention [17] integrates the Softmax and linear attention. While these methods have proven effective, their capacity to model complex patterns remains limited when compared to Softmax attention. Moreover, they operate exclusively on a single scale, neglecting the potential benefits of multi-scale feature exploration. To address these limitations, EfficientVit [4] employs depth-wise convolutions to enhance the multi-scale learning capability of linear attention. However, EfficientVit predominantly relies on small-kernel convolutions, which limits its ability to comprehensively extract multi-scale features. In this work, we propose a novel linear attention module, termed **Multi-Scale Linear Attention (MSLA)**, which is designed to learn comprehensive multi-scale features, thereby significantly enhancing the expressive power of linear attention.

3 | METHOD

In this section, we detail the proposed approach. First, we provide a concise summary of Efficient Attention. Next, we elaborate on the **Multi-Scale Linear Attention (MSLA)** module. Then, we introduce two key components: an encoder built on the MSLA module and a decoder designed to better preserve low-level spatial details while enhancing high-level semantic information. Finally, we specify the overall architecture of the proposed MSLAU-Net and its associated loss function.

3.1 | Preliminaries

Given the input $\mathbf{X} \in \mathbb{R}^{N \times C}$ with N tokens, the general form of self-attention can be written as follows in each head:

$$\begin{aligned} \mathbf{Q} &= \mathbf{X}\mathbf{W}_q, \mathbf{K} = \mathbf{X}\mathbf{W}_k, \mathbf{V} = \mathbf{X}\mathbf{W}_v, \\ \mathbf{O}_i &= \sum_{j=1}^N \frac{\text{Sim}(\mathbf{Q}_i, \mathbf{K}_j)}{\sum_{j=1}^N \text{Sim}(\mathbf{Q}_i, \mathbf{K}_j)} \mathbf{V}_j, \end{aligned} \quad (1)$$

where $\mathbf{W}_q, \mathbf{W}_k, \mathbf{W}_v \in \mathbb{R}^{C \times d}$ are learnable linear projection matrices, C and d are the channel dimension of module and each head, and $\text{Sim}(\cdot, \cdot)$ denotes the similarity function.

In modern vision transformer architectures, the most widely adopted form of attention is Softmax attention, with its similarity function defined as $\text{Sim}(\mathbf{Q}, \mathbf{K}) = \exp(\mathbf{Q}\mathbf{K}^\top / \sqrt{d})$. Softmax attention requires computing the similarity between all query-key pairs, leading to the computational complexity of $\mathcal{O}(N^2)$.

To address this issue, linear attention has been proposed as an alternative, significantly reducing the complexity. Specifically, linear attention reformulates the attention mechanism by leveraging mapping function $\phi(\cdot)$, resulting in the similarity function formulated as $\text{Sim}(\mathbf{Q}, \mathbf{K}) = \phi(\mathbf{Q})\phi(\mathbf{K})^\top$.

Efficient Attention, a type of linear attention, maintains similar representational power to Softmax attention while achieving linear computational complexity [38]. Mathematically, Efficient Attention can be expressed as follows:

$$\text{EfficientAtt}(\mathbf{Q}, \mathbf{K}, \mathbf{V}) = \text{Sim}(\mathbf{Q}, \mathbf{K})\mathbf{V} = \phi_q(\mathbf{Q})\phi_k(\mathbf{K})^\top \mathbf{V}. \quad (2)$$

The mapping functions for Efficient Attention are defined as:

$$\begin{aligned} \phi_q(\mathbf{Q}) &= \sigma_{\text{row}}(\mathbf{Q}), \\ \phi_k(\mathbf{K}) &= \sigma_{\text{col}}(\mathbf{K}), \end{aligned} \quad (3)$$

where $\sigma_{\text{row}}(\mathbf{Q}), \sigma_{\text{col}}(\mathbf{K})$ denote the application of the softmax function along each row of query matrix and each column of key matrix, respectively. Based on the associative property of matrix multiplication, the computation order can be changed from $(\phi_q(\mathbf{Q})\phi_k(\mathbf{K})^\top)\mathbf{V}$ to $\phi_q(\mathbf{Q})(\phi_k(\mathbf{K})^\top \mathbf{V})$. By doing so, the computational complexity of Efficient Attention is reduced to $\mathcal{O}(N)$.

3.2 | Multi-Scale Linear Attention

Our Multi-Scale Linear Attention (MSLA) consists of two main operational processes: Multi-Scale Feature Extraction and Linear Attention Computation. The former captures multi-scale local structural details to enhance segmentation performance. The latter leverages linear attention with an approximated global receptive field, similar to that of Softmax attention, to model long-range dependencies while improving computational efficiency. A detailed explanation is provided below.

3.2.1 | Multi-Scale Features Extraction

As illustrated in Fig. 1, we first reshape the input tokens into a feature map $\mathbf{X} \in \mathbb{R}^{\sqrt{N} \times \sqrt{N} \times C}$, and then split it into four parts along the channel dimension C :

$$\mathbf{X}_1, \mathbf{X}_2, \mathbf{X}_3, \mathbf{X}_4 = \text{Split}\left(\mathbf{X}, \frac{C}{4}\right). \quad (4)$$

After reshaping and splitting, these features are then fed into four parallel depth-wise convolution branches designed to explore multi-scale representations using 3×3 , 5×5 , 7×7 , and 9×9 kernels, respectively. Smaller convolution kernels (e.g., 3×3) excel at detecting fine-grained details in medical images, such as subtle lesion areas, while larger kernels (e.g., 9×9) are

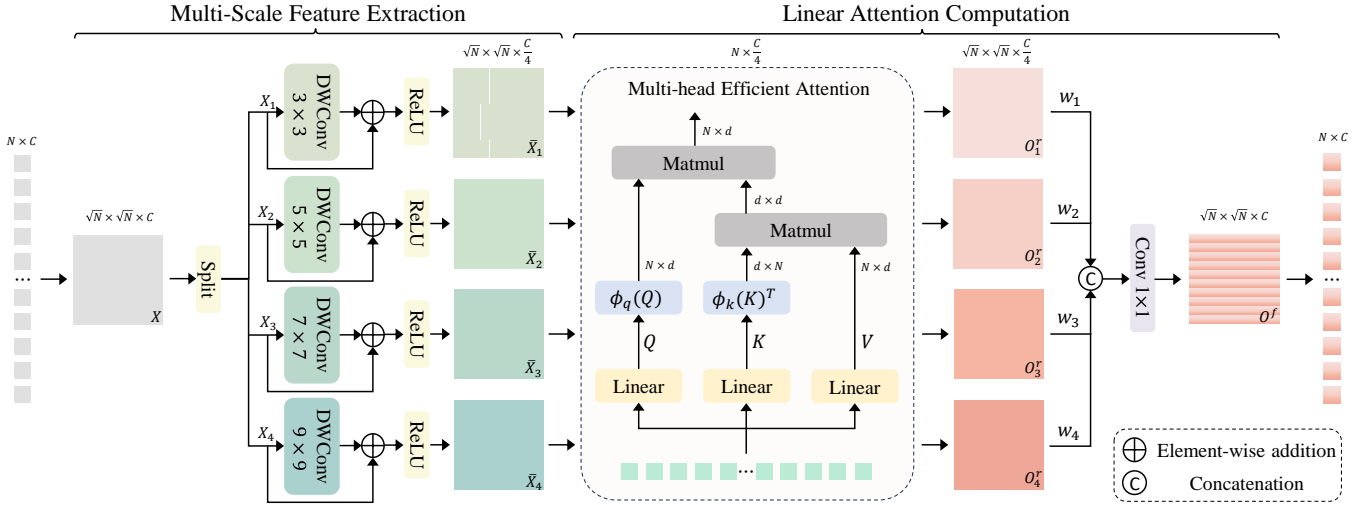


FIGURE 1 Details of Multi-Scale Linear Attention. The MSLA module is designed in parallel to take full advantage of CNNs for capturing multi-scale features and linear attention for modeling long-range dependencies. The input feature map is first divided into four parts along the channel dimension. Each part is then processed through depth-wise convolution with different kernel sizes (3×3 , 5×5 , 7×7 , and 9×9) to extract multi-scale features. Next, linear attention, i.e., Efficient Attention, is applied to the multi-scale features to model long-range dependencies. Finally, the resulting outputs are fused using a 1×1 convolution.

more effective at capturing broader structures, including the overall contours of organ.

Subsequently, the features from different scales are integrated with the original input features through residual connections, followed by a ReLU activation function. This process facilitates richer multi-scale feature representations and can be formulated as follows:

$$\bar{X}_i = \text{ReLU}(f_{k_i \times k_i}^{dwc}(X_i) + X_i), \quad (5)$$

where $i \in \{1, 2, 3, 4\}$, $k_i = 2i + 1$ and the operation $f_{k_i \times k_i}^{dwc}$ represents the depth-wise convolution with the kernel size of k_i .

3.2.2 | Linear Attention Computation

To further enhance the model's ability to locate regions of interest and suppress irrelevant information, we employ Efficient Attention [38] to capture contextual information across the multi-scale features in each branch, respectively.

First, we reshape $\bar{X}_i \in \mathbb{R}^{\sqrt{N} \times \sqrt{N} \times \frac{C}{4}}$ into $\bar{X}_i^r \in \mathbb{R}^{N \times \frac{C}{4}}$. To extract global representations, we apply Efficient Attention to the multi-scale tokens \bar{X}_i^r . Specifically, for i -th branch and h -th head, we derive the query, key, value tensor, $Q_{i,h}, K_{i,h}, V_{i,h} \in \mathbb{R}^{N \times d}$, using specific linear projections:

$$Q_{i,h} = \bar{X}_i^r W_{i,h}^q, K_{i,h} = \bar{X}_i^r W_{i,h}^k, V_{i,h} = \bar{X}_i^r W_{i,h}^v, \quad (6)$$

where $W_{i,h}^q, W_{i,h}^k, W_{i,h}^v \in \mathbb{R}^{\frac{C}{4} \times d}$ are projection weights for the query, key, value, respectively.

Next, we perform attention computation separately for each head using Efficient Attention. Formally,

$$\begin{aligned} \text{head}_{i,h} &= \text{EfficientAtt}_{i,h}(Q_{i,h}, K_{i,h}, V_{i,h}), \\ O_i &= \text{Concat}(\text{head}_{i,0}, \text{head}_{i,1}, \dots, \text{head}_{i,h-1}) W_i^o, \end{aligned} \quad (7)$$

where $\text{head}_{i,h}$ is the output of the h -th attention head in i -th branch. An additional linear transformation with weight matrix $W_i^o \in \mathbb{R}^{\frac{C}{4} \times \frac{C}{4}}$ is applied to combine the outputs from all heads.

Finally, $O_i \in \mathbb{R}^{N \times \frac{C}{4}}$ is reshaped to image representations $O_i^r \in \mathbb{R}^{\sqrt{N} \times \sqrt{N} \times \frac{C}{4}}$ on spatial dimension. This transformation facilitates subsequent convolution operations, thereby enhancing the fusion of multi-scale features. The fusion process can be described as:

$$O^f = f_{1 \times 1}([w_1 O_1^r, w_2 O_2^r, w_3 O_3^r, w_4 O_4^r]), \quad (8)$$

where w_i are learnable weight parameters, $[\cdot]$ represents the channel-wise concatenation, and $f_{1 \times 1}$ denotes a 1×1 convolution. We then reshape the fused feature map $O^f \in \mathbb{R}^{\sqrt{N} \times \sqrt{N} \times C}$ into $O \in \mathbb{R}^{N \times C}$ to obtain the final output tokens.

3.3 | Encoder

The encoder of our model consists of four stages, as shown in Fig. 4. The first two stages comprise Patch Embedding layers and Local Feature Extraction (LFE) blocks, while the last two stages incorporate Patch Embedding layers and Global Feature Extraction (GFE) blocks. Below, we provide a detailed description of the LFE block, the GFE block, and the Patch Embedding

layer. These components are progressively stacked in a hierarchical manner, forming a four-stage pyramid structure with the configuration of [4,8,11,5]. This hierarchical stacking approach ensures that both local details and global context are effectively captured, leading to more robust and comprehensive feature representations.

Following the Local UniFormer block [26], we introduce the LFE block to better leverage the local feature extraction capabilities of CNNs. The LFE block consists of three components: a 3×3 depth-wise convolution, three consecutive convolutional layers, and a Feed-Forward Network (FFN), as illustrated in Fig. 2. The 3×3 depth-wise convolution encodes relative position information, while the three consecutive convolutional layers learn local representations. Regarding the FFN, the channel dimension of its input is first expanded by a ratio of 4 through a 1×1 convolution and then restored to the original dimension using another 1×1 convolution. The LFE block can be formulated as:

$$\hat{z}_L^{l-1} = f_{3 \times 3}^{dwc}(z_L^{l-1}) + z_L^{l-1}, \quad (9)$$

$$\hat{z}_L^l = f_{1 \times 1}(f_{5 \times 5}^{dwc}(f_{1 \times 1}(\text{BN}(\hat{z}_L^{l-1})))) + \hat{z}_L^{l-1}, \quad (10)$$

$$z_L^l = \text{FFN}(\text{BN}(\hat{z}_L^l)) + \hat{z}_L^l, \quad (11)$$

where \hat{z}_L^{l-1} , \hat{z}_L^l and z_L^l represent the outputs of the depth-wise convolution, three consecutive convolutional layers and FFN module of the l -th LFE block, respectively.

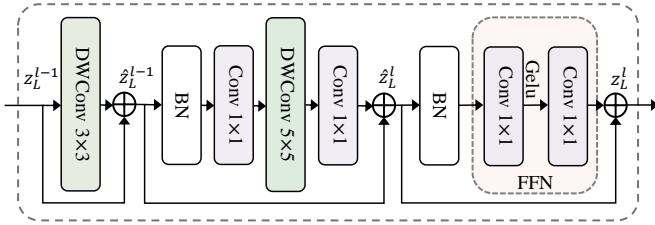


FIGURE 2 Details of the LFE block. An LFE block consists of three key modules: a 3×3 depth-wise convolution, three consecutive convolutional layers, and an FFN.

Based on the MSLA module, we design the GFE blocks to learn long-range dependencies in the deeper layers. Specifically, we employ a 3×3 depth-wise convolution at the beginning as relative position encoding. Subsequently, we sequentially apply an MSLA module and an FFN module with an expansion ratio of $e = 4$, as shown in Fig. 3. The GFE block can be expressed as:

$$\hat{z}_G^{l-1} = f_{3 \times 3}^{dwc}(z_G^{l-1}) + z_G^{l-1}, \quad (12)$$

$$\hat{z}_G^l = \text{MSLA}(\text{LN}(\hat{z}_G^{l-1})) + \hat{z}_G^{l-1}, \quad (13)$$

$$z_G^l = \text{FFN}(\text{LN}(\hat{z}_G^l)) + \hat{z}_G^l, \quad (14)$$

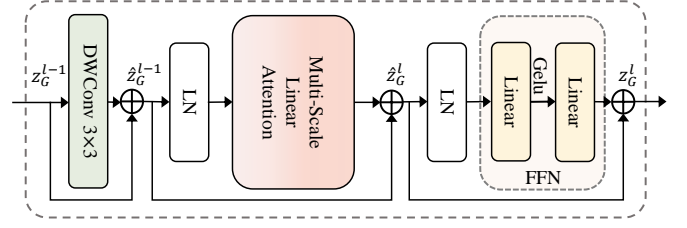


FIGURE 3 Details of the GFE Block. A GFE block comprises three main components: a 3×3 depth-wise convolution, an MSLA module, and an FFN.

where \hat{z}_G^{l-1} , \hat{z}_G^l and z_G^l represent the outputs of the depth-wise convolution, MSLA module and FFN module of the l -th GFE block, respectively.

Regarding the Patch Embedding layers, we apply a 4×4 convolution with a stride of 4 in the first stage and a 2×2 convolution with a stride of 2 in the subsequent stages. An extra Layer Normalization (LN) is added after each down-sampling convolution.

3.4 | Decoder

The decoder consists of convolution and bilinear upsampling operations, designed to perform multi-level feature aggregation and restore the resolution using a top-down feature aggregation mechanism, as shown in Fig. 4. To effectively aggregate multi-level features, we align the outputs from the second to the fourth stages of the encoder with the output of the first stage in terms of both channel dimensions and spatial resolutions. Specifically, we apply one, two, and three convolution blocks to the outputs from the second, third, and fourth stages, respectively. Each block consists of a 1×1 convolution layer followed by a bilinear upsampling layer. The 1×1 convolution layer reduces the channel dimension by half, while the bilinear upsampling layer performs $2 \times$ upsampling. This alignment is crucial for maintaining uniform feature representations across all stages, facilitating more effective multi-scale feature fusion, and improving overall model performance. After obtaining uniform channel dimensions and spatial resolutions, we sequentially perform a top-down aggregation operation on the outputs (i.e., feature maps) of the second to fourth stages using element-wise addition, thereby enhancing interactions across different stages.

Next, all aggregated feature maps with uniform channel dimensions and spatial resolutions are fed into another convolution block, which consists of two successive 3×3 convolution layers and a bilinear upsampling layer. This configuration increases the spatial resolution by $2 \times$ while keeping the channel dimension unchanged. The resulting outputs from each branch are then concatenated along the channel dimension, increasing the channel dimension by $4 \times$. Subsequently, the concatenated

feature maps are then fed into the third convolution block, which consists of a 3×3 convolution layer and a bilinear upsampling layer, to recover the full resolution $H \times W$ for predicting the final segmentation outcome.

3.5 | Architecture Overview

Our architecture, named MSLAU-Net, is a hybrid CNN-Transformer model that consists of the encoder and decoder described above. MSLAU-Net seamlessly integrates multi-scale feature extraction and multi-level feature aggregation within an encoder-decoder framework. The encoder adopts a hierarchical pyramid structure, where the first two stages consist of 4 and 8 LFE blocks, respectively, while the last two stages include 11 and 5 GFE blocks. This design ensures that our network can effectively capture both low-level local features and high-level semantic information. The decoder employs a top-down feature aggregation mechanism to integrate multi-level features from the encoder, enhancing interactions across different stages and contributing to richer feature representations. Additionally, bilinear upsampling and channel-wise concatenation are utilized to increase both the spatial resolution and channel dimensions. The entire network is carefully designed to leverage the strengths of both CNNs and transformers, ensuring efficient multi-scale feature extraction and robust multi-level feature aggregation while maintaining low computational complexity.

3.6 | Loss Function

We utilize different loss functions for each dataset in our experiments. For the CVC-ClinicDB dataset, we optimize MSLAU-Net using only the dice loss (\mathcal{L}_{dice}). It can be defined as follows:

$$\mathcal{L}_{dice} = 1 - \sum_k \frac{2\omega_k \sum_i p(k, i)g(k, i)}{\sum_i p^2(k, i) + \sum_i g^2(k, i)}, \quad (15)$$

where N is the number of pixels, $g(k, i) \in (0, 1)$ indicates the ground truth label, and $p(k, i) \in (0, 1)$ represents the predicted probability for class. K is the number of class, and $\sum_k \omega_k = 1$ is weight sum of all classes.

For the Synapse and ACDC datasets, we adopt a hybrid loss function that integrates both dice loss (\mathcal{L}_{dice}) and cross-entropy (\mathcal{L}_{ce}) loss to effectively address the issue of class imbalance. The cross-entropy loss is given by:

$$\begin{aligned} \mathcal{L}_{ce} = & -\frac{1}{N} \sum_{i=1}^N (g(k, i) \cdot \log(p(k, i)) \\ & + (1 - g(k, i)) \cdot \log(1 - p(k, i))). \end{aligned} \quad (16)$$

The overall hybrid loss function used for training on the Synapse dataset is then formulated as:

$$\mathcal{L} = \lambda \mathcal{L}_{dice} + (1 - \lambda) \mathcal{L}_{ce}, \quad (17)$$

where λ is a weighted factor that balances the impact of \mathcal{L}_{dice} and \mathcal{L}_{ce} . In our all experiments, the ω_k and λ are empirically set as $\frac{1}{K}$ and 0.6, respectively.

4 | EXPERIMENTS

4.1 | Datasets

Synapse Multi-Organ Segmentation Dataset: The dataset is sourced from the MICCAI 2015 Multi-Atlas Abdomen Labeling Challenge and consists of 30 abdominal CT scans, totaling 3,779 axial slices. Each scan has a voxel size of $([0.54-0.54] \times [0.98-0.98] \times [2.5-5.0]) \text{ mm}^3$ and contains between 85 and 198 slices, each with a resolution of 512×512 pixels. Following [6, 7], the dataset is split into 18 cases (2,212 slices) for training and 12 cases for testing. We evaluate our method by reporting the average Dice-Similarity Coefficient (DSC) and average Hausdorff Distance (HD) across eight abdominal organs: the aorta, gallbladder, spleen, left kidney, right kidney, liver, pancreas, and stomach.

Automated Cardiac Diagnosis Challenge Dataset: The ACDC dataset consists of MRI scans acquired from 100 patients with diverse pathologies. Each scan is manually annotated for three critical regions: left ventricle (LV), right ventricle (RV), and myocardium (MYO). The dataset is partitioned into 70 training samples, 10 validation samples, and 20 testing samples. Following [6, 7], we evaluate the performance of our method on these three cardiac structures using the average Dice Similarity Coefficient (DSC) as the evaluation metric.

CVC-ClinicDB Dataset: The dataset served as the official training dataset for the MICCAI 2015 Sub-Challenge on Automatic Polyp Detection. It comprises 612 images extracted from colonoscopy videos, which are randomly partitioned into three subsets: 490 images for training, 61 for validation, and 61 for testing. Each image in the dataset is accompanied by a ground truth mask that delineates the regions of polyps. On this dataset, we adopt the metrics include Mean Intersection over Union (mIoU), DSC, Accuracy, Precision, and Recall.

4.2 | Implementation Details

The MSLAU-Net is implemented using Python 3.10 and PyTorch 2.0. We train MSLAU-Net and its various ablation variants on an NVIDIA GeForce RTX 3090 GPU with 24 GB of memory. During the training process, the model weights are

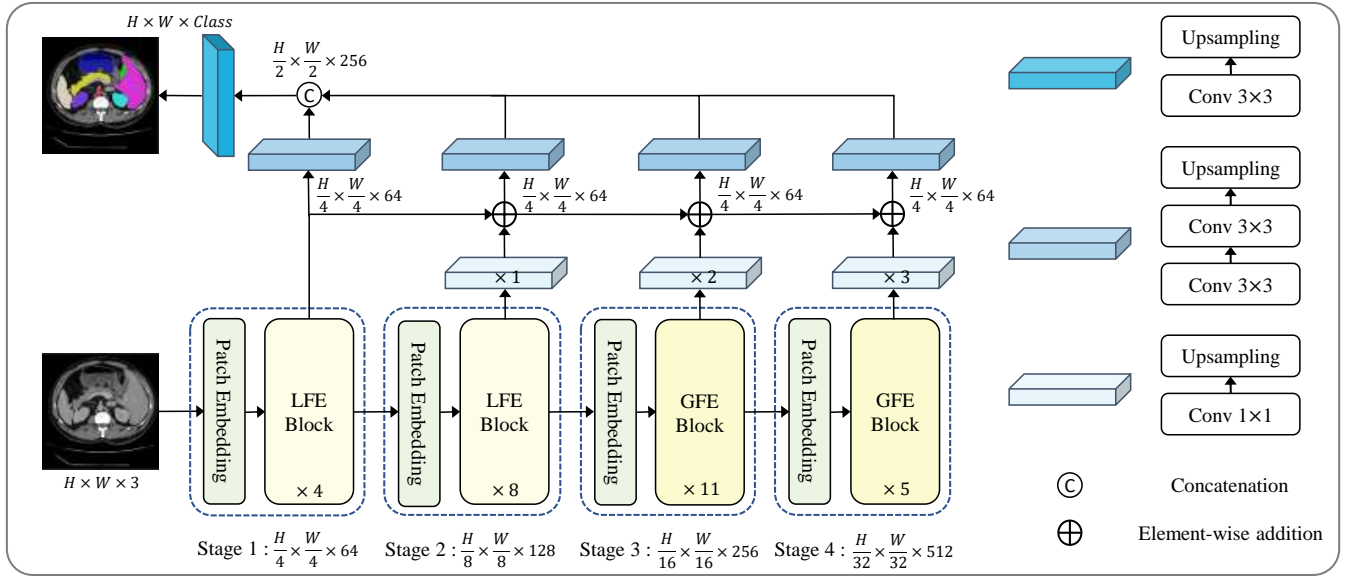


FIGURE 4 The proposed MSLAU-Net adopts an encoder-decoder structure. The encoder integrates CNN and transformer components, utilizing LFE and GFE blocks for local and global feature extraction, respectively. The decoder employs a top-down aggregation mechanism to aggregate multi-level features from the corresponding stages of the encoder. These features are then upsampled to the original image resolution, producing the final mask prediction.

initialized using pre-trained weights from ImageNet [11]. For the proposed attention mechanism, its multi-scale convolution kernels are configured as [3, 5, 7, 9] based on the results of the ablation study. For the Synapse multi-organ segmentation dataset, the input images are resized to 224×224 . The model is trained for 400 epochs using Stochastic Gradient Descent (SGD) optimizer with a batch size of 24, an initial learning rate of 0.05, a momentum of 0.9, and a weight decay of $1e-4$. Similarly, for the ACDC dataset, the input images are resized to 224×224 , but we employ the AdamW optimizer [30] with a batch size of 24, setting the initial learning rate to $3e-4$ and the weight decay to $5e-4$, training the model for 400 epochs. Additionally, for the CVC-ClinicDB dataset, the input images are resized to 256×256 . To enhance data diversity, we apply several data augmentation techniques with a probability of 0.25, including horizontal flipping, vertical flipping, rotation, and cutout. The model is then trained for 200 epochs using the AdamW optimizer with a batch size of 8, a weight decay of $5e-4$, and an initial learning rate of $1e-4$.

4.3 | Comparison on Synapse Multi-Organ Segmentation Dataset

The segmentation performance of the proposed MSLAU-Net is quantitatively evaluated on the Synapse Multi-Organ Segmentation dataset and compared to several state-of-the-art approaches. These involve CNN-based approaches such as

U-Net [36] and Att-UNet [32], Transformer-based methods like Swin-Unet [6] and MISSFormer [21], and hybrid CNN-Transformer approaches including TransUNet [7], HiFormer [19], PVT-CASCADE [34], and BRAU-Net++ [24]. The experimental results are presented in Table 1. As shown in Table 1, our method achieves the highest DSC score of 83.18%, significantly outperforming all other widely adopted techniques. This demonstrates the effectiveness of MSLAU-Net in modeling both local features and global dependencies. In terms of HD, MSLAU-Net also performs admirably, achieving a value of 17.00 mm. While this is slightly higher than the best-performing HiFormer (14.70 mm), it still reflects strong boundary localization capabilities. Furthermore, MSLAU-Net exhibits promising performance across multiple organs. Notably, it achieves the highest DSC scores for the liver (94.82%) and the right kidney (84.67%), underscoring its effectiveness in handling complex anatomical structures. Additionally, MSLAU-Net is highly parameter-efficient, with only 21.90 M parameters, making it a practical and appealing choice for real-world applications. These results show that MSLAU-Net not only achieves state-of-the-art performance but also maintains computational efficiency, positioning it as a promising solution for multi-organ segmentation tasks.

Qualitative results of different methods on the Synapse dataset are shown in Fig. 5. One can see that our method generates more accurate segmentation maps for organs such as the gallbladder, right kidney, liver, and pancreas. These results demonstrate that MSLA performs well in capturing the features

of both small and large targets. Moreover, MSLAU-Net effectively learns both local details and global semantic information, thereby yielding better segmentation results. Specifically, the proposed approach not only delineates the boundaries of organs more accurately but also maintains consistency across the entire segmentation map. These qualities highlight the effectiveness of the MSLA mechanism in enhancing the model's ability to handle complex anatomical structures.

4.4 | Comparison on Automated Cardiac Diagnosis Challenge Dataset

The comparisons of our proposed method with previous state-of-the-art methods on the ACDC dataset are given in Table 2. The results show that MSLAU-Net achieves an overall DSC of 92.13%, surpassing all other competing methods. Notably, MSLAU-Net exhibits the best performance in myocardial (Myo) and left ventricle (LV) segmentation, achieving a DSC score of 90.06% and 95.95%, highlighting its distinct advantage in handling specific regions. These findings indicate that MSLAU-Net is a highly effective and robust model for cardiac image segmentation tasks.

4.5 | Comparison on CVC-ClinicDB Dataset

According to the comparative experimental results in Table 3, MSLAU-Net exhibits outstanding segmentation performance on the CVC-ClinicDB dataset. The method achieves a mIoU of 88.68 and a DSC of 93.03%, while also excelling in other key metrics such as accuracy, precision, and recall. Furthermore, as illustrated in Fig. 6, the segmentation results produced by MSLAU-Net closely align with the ground truth. These results confirm the robust capability and high reliability of MSLAU-Net in handling complex medical image segmentation tasks.

4.6 | Ablation Study

In this section, we conduct extensive ablation studies on the Synapse dataset to investigate the impact of each component involved in MSLAU-Net. Specifically, we analyze the effectiveness of pre-trained weights, different scale combinations within the MSLA module, structure designs in the encoder, and model scale. All experiments related to the last three components, namely different scale combinations, structure designs in the encoder, and model scale, are trained from scratch.

4.6.1 | Effectiveness of Pre-trained Weights

To evaluate the specific effectiveness of pre-trained weights on improving model performance, we conduct an ablation study on Synapse dataset. As shown in Table 4, when no pre-trained weights are used (i.e., random initialization), the method have to learn all parameters from scratch, resulting in inferior performance compared to the case where pre-trained weights are utilized. In contrast, initializing the model with weights pre-trained on ImageNet significantly enhanced its performance. Specifically, the DSC is improved by approximately 3.77%, and the HD is reduced by 5.88 mm. Due to resource limitations, the following ablation studies are conducted without using pre-trained weights.

4.6.2 | Effectiveness of Different Scale Combinations in MSLA

We conduct a detailed ablation study to evaluate the impact of different scale combinations in MSLA on segmentation performance. Specifically, we first assess the performance without employing any multi-scale strategy, i.e., using only Efficient Attention, which achieves a DSC of 77.76% and an HD of 27.27 mm. Subsequently, we explore dual-branch and four-branch multi-scale strategies, where convolution kernel sizes 1, 3, 5, 7, and 9 are used in different combinations. The results are shown in Table 5. It can be seen that in the dual-branch strategy, the best performance is achieved with kernel sizes 5 and 7, resulting in a DSC of 78.32% and an HD of 24.92 mm, while for the four-branch strategy, setting the kernel sizes to [3, 5, 7, 9] yields relatively optimal performance, achieving a DSC of 79.41% and an HD of 22.88 mm. These results indicate that incorporating a multi-scale design, particularly the four-branch strategy, significantly enhances the performance of Efficient Attention. The improvement can be attributed to the ability of multi-scale strategies to capture features at various levels of detail.

4.6.3 | Effectiveness of Structure Designs within Encoder

We conduct an ablation study to evaluate the effectiveness of different configurations of LFE and GFE blocks stage by stage within the encoder. The results are presented in Table 6. One can see that using only LFE blocks (i.e., the configuration LLLL) or only GFE blocks (i.e., the configuration GGGG) for all stages yields relatively low performance. The best segmentation performance is achieved with the configuration LLGG. The phenomena reveal that while transformers excel at global feature modeling, they are relatively less effective than CNNs in extracting local representations, potentially leading to redundant

TABLE 1 Quantitative results of our approach against other state-of-the-art methods on Synapse multi-organ segmentation dataset. The symbol \uparrow indicates the larger the better. The symbol \downarrow denotes the smaller the better. The best result is in **bold**, and the second best is underlined.

| Methods | Params (M) | DSC (%) \uparrow | HD (mm) \downarrow | Aorta | Gallbladder | Kidney (L) | Kidney (R) | Liver | Pancreas | Spleen | Stomach |
|------------------|------------|--------------------|----------------------|--------------|--------------|--------------|--------------|--------------|--------------|--------------|--------------|
| U-Net [36] | 14.80 | 76.85 | 39.70 | <u>89.07</u> | 69.72 | 77.77 | 68.60 | 93.43 | 53.98 | 86.67 | 75.58 |
| Att-UNet [32] | 34.88 | 77.77 | 36.02 | 89.55 | 68.88 | 77.98 | 71.11 | 93.57 | 58.04 | 87.30 | 75.75 |
| TransUNet [7] | 105.28 | 77.48 | 31.69 | 87.23 | 63.13 | 81.87 | 77.02 | 94.08 | 55.86 | 85.08 | 75.62 |
| Swin-UNet [6] | 27.17 | 79.13 | 21.55 | 85.47 | 66.53 | 83.28 | 79.61 | 94.29 | 56.58 | 90.66 | 76.60 |
| HiFormer [19] | 25.51 | 80.39 | 14.70 | 86.21 | 65.69 | 85.23 | 79.77 | 94.61 | 59.52 | 90.99 | 81.08 |
| PVT-CASCADE [34] | 35.28 | 81.06 | 20.23 | 83.01 | <u>70.59</u> | 82.23 | 80.37 | 94.08 | 64.43 | 90.10 | 83.69 |
| MISSFormer [21] | 42.46 | 81.96 | 18.20 | 86.99 | 68.65 | <u>85.21</u> | <u>82.00</u> | 94.41 | <u>65.67</u> | 91.92 | 80.81 |
| BRAU-Net++ [24] | 62.63 | <u>82.47</u> | 19.07 | 87.95 | 69.10 | 87.13 | 81.53 | <u>94.71</u> | 65.17 | <u>91.89</u> | <u>82.26</u> |
| MSLAU-Net (Ours) | 21.90 | 83.18 | <u>17.00</u> | 88.68 | 73.95 | <u>85.54</u> | 84.57 | 94.82 | 65.79 | 91.2 | 80.87 |

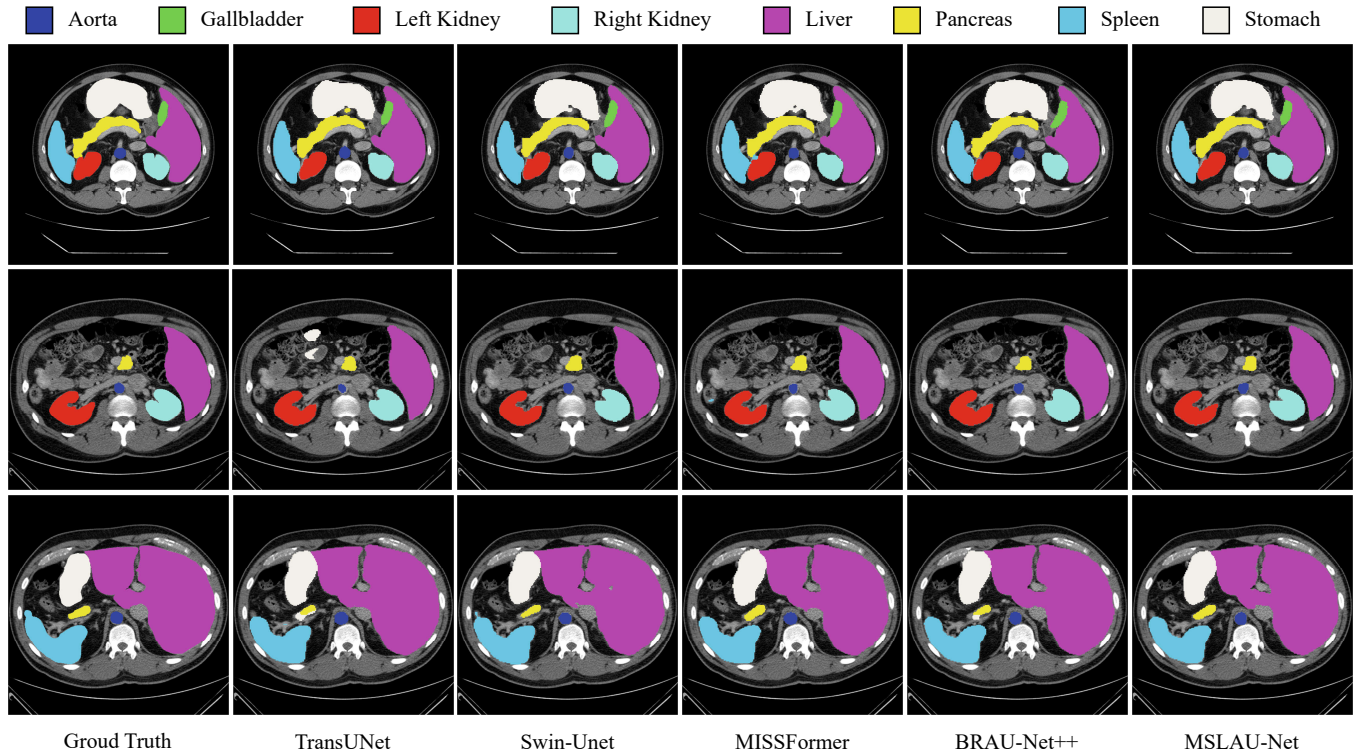


FIGURE 5 Qualitative results of different methods on the Synapse multi-organ segmentation dataset. Our MSLAU-Net captures organ boundaries more accurately and demonstrates superior detail-handling capabilities. Best viewed in color with zoom-in.

TABLE 2 Qualitative results of different methods on ACDC dataset.

| Methods | DSC \uparrow | RV \uparrow | Myo \uparrow | LV \uparrow |
|------------------|----------------|---------------|----------------|---------------|
| R50+U-Net [7] | 87.55 | 87.10 | 80.63 | 94.92 |
| R50+Att-UNet [7] | 86.75 | 87.58 | 79.20 | 93.47 |
| TransUNet [7] | 89.71 | 88.86 | 84.54 | 95.73 |
| Swin-UNet [6] | 90.00 | 88.55 | 85.62 | 95.83 |
| MISSFormer [21] | 90.86 | 89.55 | 88.04 | 94.99 |
| PVT-CASCADE [34] | 91.46 | 88.90 | <u>89.97</u> | 95.50 |
| BRAU-Net++ [24] | <u>92.07</u> | 90.72 | 89.57 | <u>95.90</u> |
| MSLAU-Net (Ours) | 92.13 | <u>90.38</u> | 90.06 | 95.95 |

attention. As expected, the optimal performance is achieved by leveraging CNNs in the first two stages and transformers in the last two stages. This configuration effectively balances local detail extraction and global context understanding by leveraging the strengths of both architectures.

4.6.4 | Effectiveness of Model Scale

We use two model scales, named “Base” and “Small” models, to evaluate the impact of the model scale on segmentation

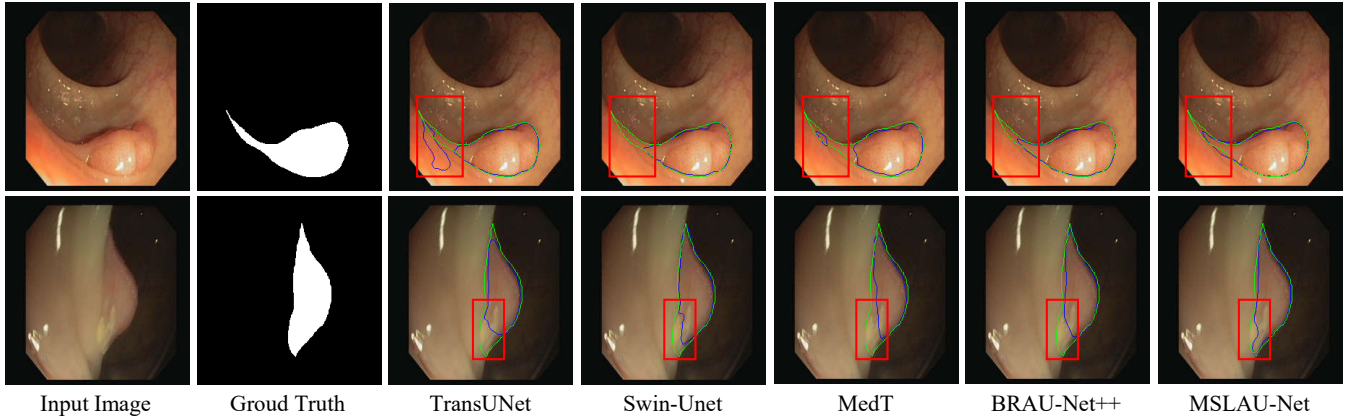


FIGURE 6 Qualitative results of different methods on the CVC-ClinicDB dataset. Ground truth boundaries are shown in green, and predicted boundaries are shown in blue. Our MSLAU-Net demonstrates better performance in matching the ground truth compared to other state-of-the-art methods. Best viewed in color with zoom-in.

TABLE 3 Qualitative results of different methods on CVC-ClinicDB dataset.

| Methods | mIoU \uparrow | DSC \uparrow | Accuracy \uparrow | Precision \uparrow | Recall \uparrow |
|------------------|-----------------|----------------|---------------------|----------------------|-------------------|
| U-Net [36] | 80.91 | 87.22 | 98.45 | 88.24 | 89.35 |
| Att-UNet [32] | 83.54 | 89.57 | 98.64 | 90.47 | 90.10 |
| MedT [40] | 81.47 | 86.97 | 98.44 | 89.35 | 90.04 |
| TransUNet [7] | 79.95 | 86.70 | 98.25 | 87.63 | 87.34 |
| Swin-Unet [6] | 84.85 | 88.21 | 98.72 | <u>90.52</u> | 91.13 |
| BRAU-Net++ [24] | <u>88.17</u> | <u>92.94</u> | <u>98.83</u> | 93.84 | 93.06 |
| MSLAU-Net (Ours) | 88.68 | 93.03 | 98.84 | 93.84 | <u>92.65</u> |

performance. Their configurations and results are presented in Table 7. We can see that despite having significantly fewer parameters (14.39 M vs. 21.90 M) and lower computational complexity (3.73 GFLOPs vs. 5.05 GFLOPs), the “Small” variant still achieves highly competitive performance (79.41% vs. 76.96% on DSC and 22.88 mm vs. 25.32 mm on HD). However, for optimal performance, we select the “Base” model as our final architecture. Additionally, it is worth noting that, due to computational resource constraints, the reported performance corresponds to the model trained without using pre-trained weights.

4.7 | Visualization

We visualize the areas of greatest concern from Stage 3 with respect to a specified query, as shown in Figure 7. For queries on organ regions, marked by red stars in the first and second slices, the module accurately focuses on the corresponding regions of the organ, as indicated by high-intensity areas in the heatmap. When the query is placed in non-organ areas in the third slice, the heatmap demonstrates that the module precisely attends to these corresponding non-organ regions.

Similarly, for queries located in the background in the fourth slice, the module exclusively focuses on the background area. These visualizations highlight the module’s ability to effectively identify and concentrate on specific target regions, which is helpful to understand how our MSLA attention module works.

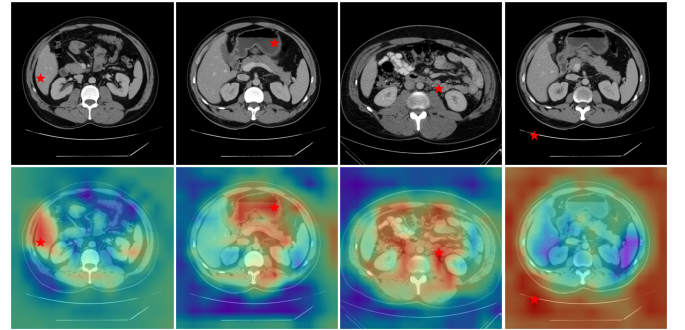


FIGURE 7 The top row presents different slices on Synapse dataset, with red stars indicating the positions of the query. The bottom row displays the corresponding attention heatmaps.

5 | CONCLUSIONS

In this paper, we propose MSLAU-Net, a hybrid CNN-Transformer architecture designed for medical image segmentation. Specifically, we introduce Multi-Scale Linear Attention (MSLA) to capture multi-scale information and perform global attention computation while maintaining low computational complexity. Additionally, we incorporate a top-down multi-level feature aggregation mechanism in the decoder, effectively

TABLE 4 Ablation study of the pre-trained weights on Synapse dataset. Here we only report the results of the “Base” model.

| Model Scale | Pre-trained | DSC (%) ↑ | HD (mm) ↓ | Aorta | Gallbladder | Kidney (L) | Kidney (R) | Liver | Pancreas | Spleen | Stomach |
|-------------|-------------|--------------|--------------|--------------|--------------|--------------|--------------|--------------|--------------|--------------|--------------|
| Base | w/o | 79.41 | 22.88 | 87.16 | 70.26 | 82.06 | 79.11 | 94.08 | 55.73 | 90.88 | 76.02 |
| | w | 83.18 | 17.00 | 88.68 | 73.95 | 85.54 | 84.57 | 94.82 | 65.79 | 91.26 | 80.87 |

TABLE 5 Ablation study of the different scale combinations in MSLA module on Synapse dataset.

| Multi-Scale | Branches | Kernel Size | | | | | DSC (%) ↑ | HD (mm) ↓ |
|-------------|----------|-------------|---|---|---|---|--------------|--------------|
| | | 1 | 3 | 5 | 7 | 9 | | |
| w/o | - | - | - | - | - | - | 77.76 | 27.27 |
| w | 2 | ✓ | ✓ | | | | 77.55 | 26.35 |
| | | | ✓ | ✓ | | | 78.19 | 26.99 |
| | | | | ✓ | ✓ | | 78.32 | 24.92 |
| | | | | | ✓ | ✓ | 77.65 | 24.89 |
| | 4 | ✓ | ✓ | ✓ | ✓ | ✓ | <u>78.21</u> | <u>21.84</u> |
| | | | ✓ | ✓ | ✓ | ✓ | 79.41 | 22.88 |

TABLE 6 Ablation study of encoder structure designs on the Synapse dataset. “L” represents the LFE block, “G” indicates the GFE block, and “S” denotes Stage.

| Types | | | | Params (M) | FLOPs (G) | DSC (%) ↑ | HD (mm) ↓ |
|-------|----|----|----|------------|-----------|--------------|--------------|
| S1 | S2 | S3 | S4 | | | | |
| L | L | L | L | 23.34 | 5.02 | 77.34 | 27.16 |
| L | L | L | G | 22.39 | 5.02 | 78.55 | 24.94 |
| L | L | G | G | 21.90 | 5.05 | 79.41 | 22.88 |
| L | G | G | G | 21.81 | 5.10 | 78.67 | 23.54 |
| G | G | G | G | 21.81 | 5.14 | 76.80 | 29.66 |

TABLE 7 Ablation study of the model scale on Synapse dataset.

| Model Scales | Depths | Params (M) | FLOPs (G) | DSC (%) ↑ | HD (mm) ↓ |
|--------------|------------|------------|-----------|--------------|--------------|
| Small | [3,4,8,3] | 14.39 | 3.73 | 76.96 | 25.32 |
| Base | [4,8,11,5] | 21.90 | 5.05 | 79.41 | 22.88 |

fusing high-level semantic information with low-level details to enhance segmentation accuracy. Experimental results demonstrate that our method achieves state-of-the-art performance on the Synapse multi-organ segmentation, ACDC, and CVC-ClinicDB datasets, validating its effectiveness and robustness. In future work, we aim to further improve this method by designing more efficient linear attention mechanisms, thereby enhancing its computational efficiency and robustness in handling complex pathological structures.

REFERENCES

1. J. Bernal, F. J. Sánchez, G. Fernández-Esparrach, D. Gil, C. Rodríguez, and F. Vilarino, *Wm-dova maps for accurate polyp highlighting in colonoscopy: Validation vs. saliency maps from physicians*, *Computerized medical imaging and graphics* **43** (2015), 99–111.
2. O. Bernard et al., *Deep learning techniques for automatic mri cardiac multi-structures segmentation and diagnosis: is the problem solved?*, *IEEE transactions on medical imaging* **37** (2018), no. 11, 2514–2525.
3. D. Bolya, C.-Y. Fu, X. Dai, P. Zhang, and J. Hoffman, *Hydra attention: Efficient attention with many heads*, *European conference on computer vision*, Springer, 2022, 35–49.
4. H. Cai, J. Li, M. Hu, C. Gan, and S. Han, *Efficientvit: Lightweight multi-scale attention for high-resolution dense prediction*, *Proceedings of the IEEE/CVF international conference on computer vision*, 2023, 17302–17313.
5. P. Cai, L. Jiang, Y. Li, X. Liu, and L. Lan, *Pubic symphysis-fetal head segmentation network using bifurmer attention mechanism and multi-path dilated convolution*, *International Conference on Multimedia Modeling*, Springer, 2024, 243–256.
6. H. Cao, Y. Wang, J. Chen, D. Jiang, X. Zhang, Q. Tian, and M. Wang, *Swin-UNET: Unet-like pure transformer for medical image segmentation*, *European conference on computer vision*, Springer, 2022, 205–218.
7. J. Chen et al., *Transunet: Transformers make strong encoders for medical image segmentation*, *arXiv preprint arXiv:2102.04306* (2021).
8. L.-C. Chen, G. Papandreou, I. Kokkinos, K. Murphy, and A. L. Yuille, *DeepLab: Semantic image segmentation with deep convolutional nets, atrous convolution, and fully connected crfs*, *IEEE transactions on pattern analysis and machine intelligence* **40** (2017), no. 4, 834–848.
9. L.-C. Chen, Y. Zhu, G. Papandreou, F. Schroff, and H. Adam, *Encoder-decoder with atrous separable convolution for semantic image segmentation*, *Proceedings of the European conference on computer vision (ECCV)*, 2018, 801–818.
10. Ö. Çiçek, A. Abdulkadir, S. S. Lienkamp, T. Brox, and O. Ronneberger, *3d u-net: learning dense volumetric segmentation from sparse annotation*, *Medical Image Computing and Computer-Assisted Intervention–MICCAI 2016: 19th International Conference, Athens, Greece, October 17–21, 2016, Proceedings, Part II 19*, Springer, 2016, 424–432.
11. J. Deng, W. Dong, R. Socher, L.-J. Li, K. Li, and L. Fei-Fei, *Imagenet: A large-scale hierarchical image database*, *2009 IEEE conference on computer vision and pattern recognition*, Ieee, 2009, 248–255.
12. A. Dosovitskiy et al., *An image is worth 16x16 words: Transformers for image recognition at scale*, *arXiv preprint arXiv:2010.11929* (2020).
13. H. Du, J. Wang, M. Liu, Y. Wang, and E. Meijering, *Swinpa-net: Swin transformer-based multiscale feature pyramid aggregation network for medical image segmentation*, *IEEE Transactions on Neural Networks and Learning Systems* **35** (2022), no. 4, 5355–5366.
14. Y. Gao, M. Zhou, and D. N. Metaxas, *Unet: a hybrid transformer architecture for medical image segmentation*, *Medical image computing and computer assisted intervention–MICCAI 2021: 24th international conference, Strasbourg, France, September 27–October 1, 2021, proceedings, Part III 24*, Springer, 2021, 61–71.
15. Z. Gu et al., *Ce-net: Context encoder network for 2d medical image segmentation*, *IEEE transactions on medical imaging* **38** (2019), no. 10, 2281–2292.
16. D. Han, X. Pan, Y. Han, S. Song, and G. Huang, *Flatten transformer: Vision transformer using focused linear attention*, *Proceedings of the IEEE/CVF international conference on computer vision*, 2023, 5961–5971.
17. D. Han et al., *Agent attention: On the integration of softmax and linear attention*, *European Conference on Computer Vision*, Springer, 2024, 124–140.

18. A. Hatamizadeh et al., *Unetr: Transformers for 3d medical image segmentation*, *Proceedings of the IEEE/CVF winter conference on applications of computer vision*, 2022, 574–584.
19. M. Heidari, A. Kazerouni, M. Soltany, R. Azad, E. K. Aghdam, J. Cohen-Adad, and D. Merhof, *Hiformer: Hierarchical multi-scale representations using transformers for medical image segmentation*, *Proceedings of the IEEE/CVF winter conference on applications of computer vision*, 2023, 6202–6212.
20. H. Huang et al., *Unet 3+: A full-scale connected unet for medical image segmentation*, *ICASSP 2020-2020 IEEE international conference on acoustics, speech and signal processing (ICASSP)*, IEEE, 2020, 1055–1059.
21. X. Huang, Z. Deng, D. Li, and X. Yuan, *Missformer: An effective medical image segmentation transformer*, arXiv preprint arXiv:2109.07162 (2021).
22. W. Jiang, M. Liu, Y. Peng, L. Wu, and Y. Wang, *Hdcb-net: A neural network with the hybrid dilated convolution for pixel-level crack detection on concrete bridges*, *IEEE Transactions on Industrial Informatics* **17** (2020), no. 8, 5485–5494.
23. A. Katharopoulos, A. Vyas, N. Pappas, and F. Fleuret, *Transformers are rnns: Fast autoregressive transformers with linear attention*, *International conference on machine learning*, PMLR, 2020, 5156–5165.
24. L. Lan, P. Cai, L. Jiang, X. Liu, Y. Li, and Y. Zhang, *Braunet++: U-shaped hybrid cnn-transformer network for medical image segmentation*, arXiv preprint arXiv:2401.00722 (2024).
25. B. Landman, Z. Xu, J. Igelsias, M. Styner, T. Langerak, and A. Klein, *Miccai multi-atlas labeling beyond the cranial vault—workshop and challenge*, *Proc. MICCAI multi-atlas labeling beyond cranial vault—workshop challenge*, vol. 5, Munich, Germany, 2015, 12.
26. K. Li et al., *Uniformer: Unifying convolution and self-attention for visual recognition*, *IEEE Transactions on Pattern Analysis and Machine Intelligence* **45** (2023), no. 10, 12581–12600.
27. X. Li, H. Chen, X. Qi, Q. Dou, C.-W. Fu, and P.-A. Heng, *H-denseunet: hybrid densely connected unet for liver and tumor segmentation from ct volumes*, *IEEE transactions on medical imaging* **37** (2018), no. 12, 2663–2674.
28. Z. Liu et al., *Swin transformer: Hierarchical vision transformer using shifted windows*, *Proceedings of the IEEE/CVF international conference on computer vision*, 2021, 10012–10022.
29. J. Long, E. Shelhamer, and T. Darrell, *Fully convolutional networks for semantic segmentation*, *Proceedings of the IEEE conference on computer vision and pattern recognition*, 2015, 3431–3440.
30. I. Loshchilov and F. Hutter, *Decoupled weight decay regularization*, arXiv preprint arXiv:1711.05101 (2017).
31. F. Milletari, N. Navab, and S.-A. Ahmadi, *V-net: Fully convolutional neural networks for volumetric medical image segmentation*, *2016 fourth international conference on 3D vision (3DV)*, Ieee, 2016, 565–571.
32. O. Oktay et al., *Attention u-net: Learning where to look for the pancreas*, arXiv preprint arXiv:1804.03999 (2018).
33. C. Peng and J. Ma, *Semantic segmentation using stride spatial pyramid pooling and dual attention decoder*, *Pattern Recognition* **107** (2020), 107498.
34. M. M. Rahman and R. Marculescu, *Medical image segmentation via cascaded attention decoding*, *Proceedings of the IEEE/CVF winter conference on applications of computer vision*, 2023, 6222–6231.
35. M. M. Rahman, M. Munir, and R. Marculescu, *Emcad: Efficient multi-scale convolutional attention decoding for medical image segmentation*, *Proceedings of the IEEE/CVF Conference on Computer Vision and Pattern Recognition*, 2024, 11769–11779.
36. O. Ronneberger, P. Fischer, and T. Brox, *U-net: Convolutional networks for biomedical image segmentation*, *Medical image computing and computer-assisted intervention—MICCAI 2015: 18th international conference, Munich, Germany, October 5-9, 2015, proceedings, part III 18*, Springer, 2015, 234–241.
37. J. Schlemper, O. Oktay, M. Schaap, M. Heinrich, B. Kainz, B. Glocker, and D. Rueckert, *Attention gated networks: Learning to leverage salient regions in medical images*, *Medical image analysis* **53** (2019), 197–207.
38. Z. Shen, M. Zhang, H. Zhao, S. Yi, and H. Li, *Efficient attention: Attention with linear complexities*, *Proceedings of the IEEE/CVF winter conference on applications of computer vision*, 2021, 3531–3539.
39. A. Srivastava et al., *Msrf-net: a multi-scale residual fusion network for biomedical image segmentation*, *IEEE Journal of Biomedical and Health Informatics* **26** (2021), no. 5, 2252–2263.
40. J. M. J. Valanarasu, P. Oza, I. Hacıhaliloglu, and V. M. Patel, *Medical transformer: Gated axial-attention for medical image segmentation*, *Medical image computing and computer assisted intervention—MICCAI 2021: 24th international conference, Strasbourg, France, September 27–October 1, 2021, proceedings, part I 24*, Springer, 2021, 36–46.
41. A. Vaswani et al., *Attention is all you need*, *Advances in neural information processing systems* **30** (2017).
42. X. Wang, R. Girshick, A. Gupta, and K. He, *Non-local neural networks*, *Proceedings of the IEEE conference on computer vision and pattern recognition*, 2018, 7794–7803.
43. E. Xie, W. Wang, Z. Yu, A. Anandkumar, J. M. Alvarez, and P. Luo, *Segformer: Simple and efficient design for semantic segmentation with transformers*, *Advances in neural information processing systems* **34** (2021), 12077–12090.
44. H. Zhao, J. Shi, X. Qi, X. Wang, and J. Jia, *Pyramid scene parsing network*, *Proceedings of the IEEE conference on computer vision and pattern recognition*, 2017, 2881–2890.
45. H.-Y. Zhou, J. Guo, Y. Zhang, X. Han, L. Yu, L. Wang, and Y. Yu, *nn-former: volumetric medical image segmentation via a 3d transformer*, *IEEE transactions on image processing* **32** (2023), 4036–4045.
46. Z. Zhou, M. M. Rahman Siddiquee, N. Tajbakhsh, and J. Liang, *Unet++: A nested u-net architecture for medical image segmentation*, *Deep learning in medical image analysis and multimodal learning for clinical decision support: 4th international workshop, DLMIA 2018, and 8th international workshop, ML-CDS 2018, held in conjunction with MICCAI 2018, Granada, Spain, September 20, 2018, proceedings 4*, Springer, 2018, 3–11.
47. L. Zhu, X. Wang, Z. Ke, W. Zhang, and R. W. Lau, *Biformer: Vision transformer with bi-level routing attention*, *Proceedings of the IEEE/CVF conference on computer vision and pattern recognition*, 2023, 10323–10333.